

Generation of entanglement from mechanical rotation

Marko Toroš,¹ Marion Cromb,¹ Mauro Paternostro,² and Daniele Faccio¹

¹*School of Physics and Astronomy, University of Glasgow, Glasgow, G12 8QQ, United Kingdom*

²*Centre for Quantum Materials and Technologies, School of Mathematics and Physics, Queen's University, Belfast BT7 1NN, United Kingdom*

Many phenomena and fundamental predictions, ranging from Hawking radiation to the early evolution of the Universe rely on the interplay between quantum mechanics and gravity or more generally, quantum mechanics in curved spacetimes. However, our understanding is hindered by the lack of experiments that actually allow us to probe quantum mechanics in curved spacetime in a repeatable and accessible way. Here we propose an experimental scheme for a photon that is prepared in a path superposition state across two rotating Sagnac interferometers that have different diameters and thus represent a superposition of two different spacetimes. We predict the generation of genuine entanglement even at low rotation frequencies and show how these effects could be observed even due to the Earth's rotation. These predictions provide an accessible platform in which to study the role of the underlying spacetime in the generation of entanglement.

Introduction.— Our understanding of the physical world rests on two theories constructed at the beginning of the 20th century. Quantum mechanics arose out of the necessity to explain new results coming from deceitfully simple experiments [1], whilst general relativity emerged by recognizing the profound equivalence between inertial and gravitational effects [2]. Yet, despite their numerous successes, we have little experimental evidence about the regime where the two theories meet. On the one hand, quantum mechanics is well tested in the domain of elementary particles up to the scale of atoms and macromolecules [3], while, on the other hand, the experimental evidence for gravitational effects is mostly limited to much larger length scales [4].

Nonetheless, over the decades a handful of experiments began testing quantum systems in the underlying spacetime. Among the most notable are the seminal works on neutron interferometry in the Earth's gravitational field [5, 6]. These have led to a series of experiments which probe interference phenomena in the regime of Newtonian gravity [7–10] as well as to Sagnac interferometers probing non-inertial rotational motion [11, 12].

More recently, the development of photonic technologies have enabled the exploration of entanglement and multi-mode interference at the quantum-gravity interface. It has been shown that linear accelerations do not affect two-photon entanglement [13], while low-frequency rotations can modify two-photon Hong-Ou-Mandel interference [14], and that the anti-bunching signature of entanglement can be concealed or revealed by low-frequency rotations [15, 16]. These initial works suggested general relativistic adaptations [14] to satellite-based missions [17] with new generalizations under development [18–22].

Ring laser gyroscopes have also achieved exquisite sensitivities in underground facilities [23], with proposals for testing the Lense-Thirring effect [24] and for constraining theories of gravity [25], offering an alternative to orbiting cryogenic gyroscopes [26] and to satellite laser

ranging [27]. Moreover, Sagnac-based interferometers have been suggested for detecting gravitational waves from intermediate-mass black hole mergers [28], and are the backbone of fundamental and technological applications [29, 30].

The above experiments and proposals, striking in their own right, have in common that the degree of entanglement remains unaltered by the underlying spacetime. Although theoretical calculations are indicating that entanglement is not an invariant quantity in a general relativistic setting [31, 32] any variations become vanishingly small at low accelerations or in weak gravity [13]. All experimental and theoretical results are thus suggesting, at least in the regime within reach of typical laboratory experiments, that entanglement remains unaltered by the underlying spacetime.

As we show here, this is not the case: we provide a protocol for *generating entanglement* in the regime of low accelerations. We exploit a previously unexplored coupling that arises in non-inertial rotating reference frames. We will focus on an implementation with photonic systems, which offers the prospect of an experimental implementation using the path-polarization degrees of freedom. In particular, we will show that an initially separable state becomes *maximally entangled* even at low-frequency of rotations ~ 1 Hz, using fibers of length ~ 30 m, and a platform of radius ~ 0.5 m. The scheme relies on a single photon source, the original use of a dual-Sagnac interferometer – which allows for the interpretation of our results in terms of spacetime superpositions – and protocols for witnessing quantum entanglement. We discuss the implications for the quantum-gravity interface, and conclude by estimating the experimental requirements to test the generation of entanglement driven by the Earth's daily rotation.

Coupling rotations and paths. – The study of rotating reference frames has led to major breakthroughs in experimental and theoretical physics, from Sagnac's test of Special relativity [33, 34], to Einstein's General

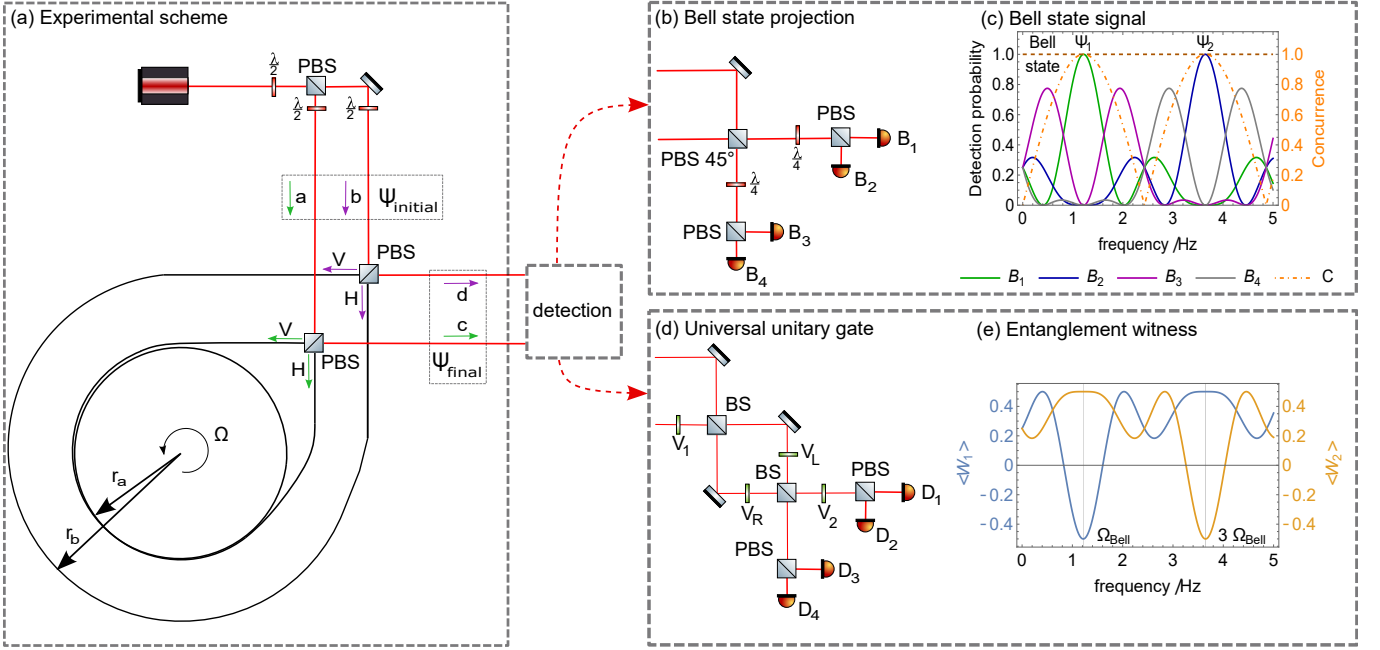


Figure 1. Scheme for generating path-polarization entanglement from mechanical rotation. **(a)** The scheme consists of a single photon source, polarizing beam splitters (PBSs), and half-wave plates (HWPs) denoted by $\lambda/2$. We consider fiber loops with radii $r_b \sim 0.5$ m, $r_a \sim r_b/2$ (with total length $l \sim 2\pi r_b N_b$ with winding number $N_b = 10$) and a photon wavelength 800 nm. The experimental setup is placed on a platform which can be set in rotation with frequency Ω . The purple and green arrows indicate the paths a, b , while the polarization is denoted by H, V . We start with a separable path-polarization photon $|\psi_{\text{initial}}\rangle$; depending on the frequency of rotation Ω the final photon $|\psi_{\text{final}}\rangle$ can remain separable or becomes entangled. We can generate a maximally entangled Bell state by tuning the frequency of the platform to $\Omega_{\text{Bell}} = \pi c^2 / (2\omega \mathcal{A})$, where ω is the mean photon frequency, and $\mathcal{A} = \Delta r l$ is the effective area of the interferometer ($\Delta r = r_b - r_a$ is the difference of the radii, and l is the path length assumed to be equal for the a, b paths). **(b)** The detector B_j measures the Bell-state ψ_j ($j = 1, \dots, 4$). The first PBS is rotated by $\pi/4$, and the quarter-wave plates (QWPs) are denoted by $\lambda/4$ (with the fast axis oriented at $\pi/4$ which transforms circular polarization to linear polarization). **(c)** The detector B_1 (B_2) measures the maximally entangled Bell-state ψ_1 (ψ_2) at frequency Ω_{Bell} ($3\Omega_{\text{Bell}}$) where the concurrence achieves the maximum possible value $C = 1$. We find $\Omega_{\text{Bell}} \sim 2\pi \times 1.2$ Hz, which can be readily achieved with similar photonic setups [14]. **(d)** Universal unitary gate for single-photon two-qubit states which can be used for tomographic reconstruction or implementing entanglement witnesses. The two beam-splitters (BSs) together with the mirrors form a Mach-Zehnder interferometer, and V_j ($j = 1, R, L, 2$) denotes an optical element composed of a HWP, two enclosing QWPs, and a phase shifter. **(e)** Optimal entanglement witnesses \mathcal{W}_1 (\mathcal{W}_2) for the maximally entangled Bell-state ψ_1 (ψ_2) as a function of rotation frequency. Entanglement is witnessed when $\mathcal{W}_j < 0$ ($j = 1, 2$).

theory of relativity [35]. In this work we are interested in dynamical effects that arise from the motion of quantum systems in a rotating Minkowski spacetime.

The equations of motion can be constructed from two simple observations. First, non-inertial rotational effects scale with the frequency of rotation Ω . Second, from the viewpoint of the co-rotating observer, free-moving objects are rotating around the origin, and must thus possess an angular momentum \mathbf{J} . We are thus led to the Hamiltonian term $\sim \Omega \cdot \mathbf{J}$ [36]. The situation further simplifies for motion on a circle with the axis of rotation located at the origin of the coordinates [15]

$$H_{\text{rot}} = H + \Omega r p, \quad (1)$$

where H is the usual Hamiltonian that is present already in an inertial reference frame, and r (p) is the radial position (tangential momentum) of the system.

Let us now consider the motion of photons in such a rotating spacetime. We can gain an intuitive understanding of Eq. (1) by recalling the relation between energy and momentum [37, 38], $p = \pm H / (nc)$, where n is the refractive index of the medium, and c is the speed of light. The Hamiltonian hence transforms to $H_{\text{rot}}^{(\pm)} = H(1 \pm \frac{\Omega r}{nc})$, where $\pm \frac{\Omega r}{nc}$ can be seen as the Doppler shift of the energy due to the rotational motion (with the sign indicating counter-rotating/co-rotating motion with respect to the platform). It is precisely this imbalance between the two directions of motion that is responsible for the Sagnac phase, $\phi_s = (H_{\text{rot}}^{(+)} - H_{\text{rot}}^{(-)})t/\hbar = 2H\Omega r t / (\hbar nc)$, where t is the time of flight. In particular, setting $H = \hbar\omega$ and $t = 2\pi r / (c/n)$, we then readily find the usual expression for the Sagnac phase [39]

$$\phi_s = \frac{4\Omega\omega\mathcal{A}_s}{c^2}, \quad (2)$$

where ω is the optical frequency, and $\mathcal{A}_s = \pi r^2$ denotes area enclosed by the interferometer.

The term $\Omega r p$ in Eq. (1) can be also viewed as a *coupling* between the position, r , and the momentum, p , with the values depending on the path followed by the photon. In a non-rotating reference frame $\Omega = 0$ and the coupling vanishes. As we will see, this coupling can be exploited to entangle the path-polarization degrees of freedom of photons.

Experimental scheme. – The experimental setup is shown in Fig. 1 (a). We consider the initial state

$$|\psi_{\text{initial}}\rangle = \frac{1}{2}(|a\rangle + |b\rangle)(|H\rangle + |V\rangle), \quad (3)$$

where a, b denote the path, and H, V denote the polarization (cf. Sec. A of the Supplementary Material accompanying the manuscript for more details). We note that the initial state is separable into a path part, $(|a\rangle + |b\rangle)/\sqrt{2}$, and a polarization part $(|H\rangle + |V\rangle)/\sqrt{2}$.

We then send the photon into *four* different paths with different radii and momenta, namely (r_a, p) , $(r_a, -p)$, (r_b, p) , and $(r_b, -p)$. As a consequence, the non-inertial rotational motion, via the coupling $\Omega r p$ in Eq. (1), induces four different phases in $|\psi_{\text{initial}}\rangle$. In particular, we find the final state

$$|\psi_{\text{final}}\rangle = \frac{1}{2} \left(|a\rangle [e^{-\frac{i\Omega r_a p t}{\hbar}} |H\rangle + e^{\frac{i\Omega r_a p t}{\hbar}} |V\rangle] + |b\rangle [e^{-\frac{i\Omega r_b p t}{\hbar}} |H\rangle + e^{\frac{i\Omega r_b p t}{\hbar}} |V\rangle] \right), \quad (4)$$

where $t = nl/c$ is the the flight time with n the refractive index of the fiber, l the length of the fibers (assumed equal for the two paths), c the speed of light, $p = E/(nc) = \hbar\omega/(nc)$ the momentum, and ω the photon frequency. We note that the phases can be rewritten as

$$\phi_j \equiv \frac{\Omega r_j p t}{\hbar} = \frac{\Omega \omega \mathcal{A}_j}{c^2}, \quad (j = a, b) \quad (5)$$

where $\mathcal{A}_j = r_j l$ is an effective area of the loop. The phases ϕ_j can thus be seen as variants of the Sagnac phase introduced in Eq. (2). Importantly, such phases do not depend on the refractive index of the medium, indicating that the effect highlighted here does not stem from light-matter coupling in the fibers but rather that it is rooted in relativity [39–41].

Let us consider first the case $\Omega = 0$. We note that the final state in Eq. (4) reduces to the initial state in Eq. (3) and thus a non-rotating platform has no effect on entanglement, as expected. Conversely when $\Omega \neq 0$ the state in Eq. (4) will in general become entangled (as we can no longer write it as the product of the path and polarization states). The effect of mechanical rotation is to rotate the polarization state depending on the photon path a, b – as we will see the polarization states in Eq. (4) associated to

paths a and b can become orthogonal (the overall polarization states in the square brackets), resulting in a maximally entangled path-polarization state. This shows that non-inertial rotating motion generates entanglement.

Spacetime superpositions. – The presented mechanism for the generation of entanglement, arising from the ostensibly relativistic Sagnac effect [39–41], poses fundamental questions about role of the underlying spacetime. Although the final state in Eq. (4) can be derived within the framework of quantum field theory in curved spacetime, the two rotating Sagnac interferometers shown in Fig. 1 are suggestive of an interpretation in terms of spacetime superpositions. This can be put in a mathematical form by modelling the spacetimes inside the two fiber loops. The metric is given by [15]:

$$ds_j^2 = c^2 \left(1 - \frac{\Omega^2 r_j^2}{c^2} \right) dt^2 - 2\Omega r_j^2 dt d\phi - r_j^2 d\phi^2, \quad (j = a, b) \quad (6)$$

where the time t and polar angle ϕ are the two coordinates, and the subscripts a (b) denote the small (big) fiber loop. The 1+1 metric in Eq. (6) is fully specified by two quantities: the angular frequency of rotation Ω and the radius r_j . Together, they encode the specific relative angular momentum Ωr_j^2 in the $dt d\phi$ term, and the factor $\Omega^2 r_j^2/c^2$, responsible for time dilation, in the dt^2 term [42, 43]. To account for these two effects, which are properties of the spacetime and not of the photons, we introduce the states $|r_j, \Omega\rangle$ ($j = a, b$).

As the photon enters the two fiber loops we are thus led to consider the following joint photon-spacetime state:

$$|\psi\rangle = \frac{1}{2} (|a\rangle |r_a, \Omega\rangle + |b\rangle |r_b, \Omega\rangle) (|p\rangle |H\rangle + |-p\rangle |V\rangle), \quad (7)$$

where $|r_j, \Omega\rangle$ ($j = a, b$) denotes the state associated to the metric in Eq. (6), and $|\pm p\rangle$ is the photon momentum state. The state $|a\rangle |H\rangle$ appearing in Eqs. (3) and (4) can be thus seen as a shorthand notation for the photon-spacetime state $|a\rangle |r_a, \Omega\rangle |p\rangle |H\rangle$ (and similarly for the other three states $|a\rangle |V\rangle$, $|b\rangle |H\rangle$, and $|b\rangle |V\rangle$).

In particular, the term $|a\rangle |r_a, \Omega\rangle + |b\rangle |r_b, \Omega\rangle$ in Eq. (7) can be interpreted as a superposition of spacetimes associated to the two Sagnac interferometers. The state of the metric $|r_j, \Omega\rangle$ ($j = a, b$) will induce phases proportional to $r_j \Omega$, which is a key ingredient in entangling the path-polarization degrees of freedom of the photon. Hence, by promoting the metric in Eq. (6) to a quantum state we have shown that the generation of entanglement can be linked to the concept reminiscent of quantum reference frames [44, 45].

Maximizing entanglement. – The state in Eq. (4) will become maximally entangled when the overall polarization states in the square brackets of Eq. (4) become orthogonal. This is achieved when the overlap S between such states reduces to zero. Using the orthonormality of the $|H\rangle, |V\rangle$ polarization states, we find

$$S = \frac{1}{2} [e^{i\phi_a} \langle H | + e^{-i\phi_a} \langle V |] [e^{-i\phi_b} | H \rangle + e^{i\phi_b} | V \rangle] \quad (8)$$

$$= \cos(\Omega\omega\Delta r l / c^2),$$

where we have set $pt/\hbar = \omega l / c^2$ ($\Delta r = r_b - r_a$ is the difference of the radii, and l is the path length assumed to be equal for the a, b paths). We thus have $S = 0$ (and the path-polarization state becomes maximally entangled) when the rotation frequency Ω takes the values

$$\Omega_{\text{Bell}} \equiv \frac{(2k+1)\pi c^2}{2\omega\mathcal{A}}, \quad (k \in \mathbb{Z}) \quad (9)$$

where $\mathcal{A} = \Delta r l$ is the effective area of the interferometer. If we set the rotation frequency Ω to any odd frequency multiple of Ω_{Bell} we will also generate a maximally entangled Bell state, while if we tune Ω to any even frequency multiple of Ω_{Bell} , the state remains separable. We find the Bell states

$$|\psi_1\rangle = \frac{1}{2} \left(|a\rangle [e^{-i\frac{\pi}{2}\frac{r_a}{\Delta r}} |H\rangle + e^{i\frac{\pi}{2}\frac{r_a}{\Delta r}} |V\rangle] \right. \quad (10)$$

$$\left. + |b\rangle [e^{-i\frac{\pi}{2}\frac{r_b}{\Delta r}} |H\rangle + e^{i\frac{\pi}{2}\frac{r_b}{\Delta r}} |V\rangle] \right)$$

at $\Omega/\Omega_{\text{Bell}} = \dots, -7, -3, 1, 5, \dots$, and

$$|\psi_2\rangle = \frac{1}{2} \left(|a\rangle [e^{-i\frac{3\pi}{2}\frac{r_a}{\Delta r}} |H\rangle + e^{i\frac{3\pi}{2}\frac{r_a}{\Delta r}} |V\rangle] \right. \quad (11)$$

$$\left. + |b\rangle [e^{-i\frac{3\pi}{2}\frac{r_b}{\Delta r}} |H\rangle + e^{i\frac{3\pi}{2}\frac{r_b}{\Delta r}} |V\rangle] \right)$$

at $\Omega/\Omega_{\text{Bell}} = \dots, -5, -1, 3, 7, \dots$. Non-inertial rotational motion is thus able to generate two distinct Bell states $|\psi_1\rangle, |\psi_2\rangle$ – from an initially separable state – solely by tuning the frequency of rotation.

Verifying entanglement. – We can verify the generation of maximal entanglement using the Bell state projection scheme [46] shown in Fig. 1(b) with the experimental signature in Fig. 1(c). In particular, we compute the concurrence $C = 2|\mathbf{a}_1\mathbf{a}_4 - \mathbf{a}_2\mathbf{a}_3|$ as witness of the degree of entanglement for different rotation frequencies [47], where $\mathbf{a}_1, \dots, \mathbf{a}_4$ denote the four phase factors (including the numerical prefactor 1/2) in the order appearing in Eq. (4). When the probability of detection in B_1 or B_2 is unity then the concurrence reaches the value $C = 1$, indicating maximum entanglement (see Supplementary material B and C for more details).

We can also use the universal unitary gate for single-photon two-qubit states [48] shown in Fig. 1(d) to perform a full tomographic reconstruction or to implement a fidelity-based optimal entanglement witness [49]. The entanglement established in the system is validated whenever the entanglement witness \mathcal{W}_1 or \mathcal{W}_2 shown in Fig. 1(e) acquires a negative value (see Supplementary Material D and E for more details). In Sec. F of the Supplementary Material, we also propose an alternative experimental scheme, based on a single-loop configuration, that is capable of achieving similar results to those

reported here, but is not susceptible to alignment imperfections between the two loops (see Sec. G of Supplementary Material for a robustness analysis).

Discussion. – We have shown that path-polarization entanglement can no longer be viewed as an invariant quantity, but rather requires us to view it as a dynamical quantity that can be completely altered already by low-frequency rotations.

The literature sometimes makes a distinction between path-polarization entanglement and multi-photon entanglement. However, one can transfer intra-photon entanglement of the two separable photons to a two-photon entangled state using known entanglement swapping protocols resulting in a polarization-entangled photon pair [50, 51]. The scheme of Fig. 1 could be thus combined with entanglement swapping protocols to generate multi-photon entanglement, offering an intriguing alternative to electrodynamic protocols [52–54].

The developed scheme is also not a peculiarity of photonic systems or rotations, but readily offers the possibility of adaptations and generalizations. It can be adapted to matter-wave interferometers, as the Hamiltonian in Eq. (1) applies to any system, whether massless or massive. The scheme could also be modified to probe other gravitational couplings, such as those involving linear accelerations and spacetime curvature, although such effects are typically weaker [55] and would require a dedicated space mission [17]. Here we have focused on the strongest effect that emerges directly in a rotating reference frame in a Minkowski spacetime. The proposed scheme is thus also fundamentally different from gravitationally induced entanglement between two massive systems [56, 57], which will test the quantum nature of perturbations around the Minkowski spacetime [58–61].

Other tests of the quantum-gravity interface aim to probe specific quantum gravity phenomena [62] such as holographic fluctuations in spacetime with Michelson interferometers [63–65], modified commutation relations with optomechanical setups [66], and energy dispersion in astronomical observations [67]. There are also a number of experiments which are testing for possible violations of Lorentz invariance [68] which could arise in certain models of quantum gravity [69], and there is ongoing effort to test the Penrose wavefunction collapse [70–72] as well as other non-standard mechanisms of gravitational decoherence [73].

In summary, the scheme presented in this work addressed a hitherto unexplored process for the dynamical generation of entanglement from the underlying spacetime, which lends itself to a suggestive interpretation in terms of spacetime superpositions. Its core strength is that the predictions do not depend on specific models of quantum gravity but only on elementary notions of quantum field theory in curved spacetime. Furthermore, it is based on well-established tools from quantum optics, and it can be readily experimentally implemented using

rotational frequency ~ 1 Hz, fibers of length ~ 30 m, and a platform of radius ~ 0.5 m, similar to the numbers achieved in Ref. [14].

Even more intriguing is the fact that any rotation, even the Earth's daily one, may be used to continuously generate entanglement. Setting $\Omega_{\text{Bell}} \sim \Omega_{\text{Earth}} \sim 7 \times 10^{-5}$ Hz in Eq. (9) we find that the area required to generate maximal entanglement is about $\sim 0.65 \text{ km}^2$, which is comparable to the interferometer built by Michelson in 1925 [74, 75]. It thus appears that testing the generation of entanglement sourced by the Earth's daily rotation is well within the domain of current experimental capabilities.

Acknowledgements. – The authors acknowledge financial support from the Leverhulme Trust (grants RPG-2020-197 and RGP-2018-266), the European Union's Horizon 2020 FET-Open project TEQ (766900), the Royal Society Wolfson Fellowship (RSWF/R3/183013), the UK EPSRC (grants EP/T028424/1, EP/T00097X/1, EP/W007444/1, EP/R030413/1, EP/M01326X/1, EP/R030081/1), the Department for the Economy Northern Ireland under the US-Ireland R&D Partnership Programme, and the Royal Academy of Engineering Chair in Emerging Technologies programme.

-
- [1] Abraham Pais. Inward bound: of matter and forces in the physical world. 1986.
- [2] Abraham Pais and Stanley Goldberg. "Subtle is the Lord...": The Science and the Life of Albert Einstein, 1984.
- [3] Yaakov Y Fein, Philipp Geyer, Patrick Zwick, Filip Kialka, Sebastian Pedalino, Marcel Mayor, Stefan Gerlich, and Markus Arndt. Quantum superposition of molecules beyond 25 kda. *Nature Physics*, 15:1242, 2019.
- [4] Clifford M Will. The confrontation between general relativity and experiment. *Living reviews in relativity*, 17(1):1–117, 2014.
- [5] Roberto Colella, Albert W Overhauser, and Samuel A Werner. Observation of gravitationally induced quantum interference. *Physical Review Letters*, 34(23):1472, 1975.
- [6] SA Werner, J-L Staudenmann, and R Colella. Effect of earth's rotation on the quantum mechanical phase of the neutron. *Physical Review Letters*, 42(17):1103, 1979.
- [7] Valery V Nesvizhevsky, Hans G Börner, Alexander K Petukhov, Hartmut Abele, Stefan Bækler, Frank J Rueß, Thilo Stöferle, Alexander Westphal, Alexei M Gagarski, Guennady A Petrov, et al. Quantum states of neutrons in the earth's gravitational field. *Nature*, 415(6869):297–299, 2002.
- [8] Jeffrey B Fixler, GT Foster, JM McGuirk, and MA Kasevich. Atom interferometer measurement of the newtonian constant of gravity. *Science*, 315(5808):74–77, 2007.
- [9] Peter Asenbaum, Chris Overstreet, Tim Kovachy, Daniel D Brown, Jason M Hogan, and Mark A Kasevich. Phase shift in an atom interferometer due to spacetime curvature across its wave function. *Physical Review Letters*, 118(18):183602, 2017.
- [10] Chris Overstreet, Peter Asenbaum, Joseph Curti, Minjeong Kim, and Mark A Kasevich. Observation of a gravitational aharonov-bohm effect. *Science*, 375(6577):226–229, 2022.
- [11] Brynle Barrett, Rémy Geiger, Indranil Dutta, Matthieu Meunier, Benjamin Canuel, Alexandre Gauguier, Philippe Bouyer, and Arnaud Landragin. The sagnac effect: 20 years of development in matter-wave interferometry. *Comptes Rendus Physique*, 15(10):875–883, 2014.
- [12] Guillaume Bertocchi, Olivier Alibart, Daniel Barry Ostrowsky, Sébastien Tanzilli, and Pascal Baldi. Single-photon sagnac interferometer. *Journal of Physics B: Atomic, Molecular and Optical Physics*, 39(5):1011, 2006.
- [13] Matthias Fink, Ana Rodriguez-Aramendia, Johannes Handsteiner, Abdul Ziarkash, Fabian Steinlechner, Thomas Scheidl, Ivette Fuentes, Jacques Pienaar, Timothy C Ralph, and Rupert Ursin. Experimental test of photonic entanglement in accelerated reference frames. *Nature Communications*, 8(1):1–6, 2017.
- [14] Sara Restuccia, Marko Toroš, Graham M Gibson, Hendrik Ulbricht, Daniele Faccio, and Miles J Padgett. Photon bunching in a rotating reference frame. *Physical Review Letters*, 123(11):110401, 2019.
- [15] Marko Toroš, Sara Restuccia, Graham M Gibson, Marion Cromb, Hendrik Ulbricht, Miles Padgett, and Daniele Faccio. Revealing and concealing entanglement with non-inertial motion. *Physical Review A*, 101(4):043837, 2020.
- [16] Marion Cromb, Sara Restuccia, Graham M Gibson, Marko Toroš, Miles J Padgett, and Daniele Faccio. Controlling photon entanglement with mechanical rotation. *arXiv preprint arXiv:2210.05628*, 2022.
- [17] Juan Yin, Yuan Cao, Yu-Huai Li, Sheng-Kai Liao, Liang Zhang, Ji-Gang Ren, Wen-Qi Cai, Wei-Yue Liu, Bo Li, Hui Dai, et al. Satellite-based entanglement distribution over 1200 kilometers. *Science*, 356(6343):1140–1144, 2017.
- [18] Marco Rivera-Tapia, Marcel I Yáñez Reyes, A Delgado, and G Rubilar. Outperforming classical estimation of post-newtonian parameters of earth's gravitational field using quantum metrology. *arXiv:2101.12126*, 2021.
- [19] Anthony J Brady and Stav Haldar. Frame dragging and the hong-ou-mandel dip: Gravitational effects in multiphoton interference. *Physical Review Research*, 3(2):023024, 2021.
- [20] Sebastian P Kish and Timothy C Ralph. Quantum effects in rotating reference frames. *AVS Quantum Science*, 4(1):011401, 2022.
- [21] Roy Barzel, David Edward Bruschi, Andreas W Schell, and Claus Lämmerzahl. Observer dependence of photon bunching: The influence of the relativistic redshift on hong-ou-mandel interference. *Physical Review D*, 105(10):105016, 2022.
- [22] Thomas Mieling, Christopher Hilweg, and Philip Walther. Measuring space-time curvature using maximally path-entangled quantum states. *arXiv:2202.12562*, 2022.
- [23] Angela D Di Virgilio, Carlo Altucci, Francesco Bajardi, Andrea Basti, Nicolò Beverini, Salvatore Capozziello, Giorgio Carelli, Donatella Ciampini, Francesco Fuso, Umberto Giacomelli, et al. Sensitivity limit investigation of a sagnac gyroscope through linear regression analysis. *The European Physical Journal C*, 81(5):1–9, 2021.

- [24] Angela DV Di Virgilio, Jacopo Belfi, Wei-Tou Ni, Nicolo Beverini, Giorgio Carelli, Enrico Maccioni, and Alberto Porzio. Ginger: A feasibility study. *The European Physical Journal Plus*, 132(4):1–12, 2017.
- [25] Salvatore Capozziello, Carlo Altucci, Francesco Bajardi, Andrea Basti, Nicolò Beverini, Giorgio Carelli, Donatella Ciampini, Angela DV Di Virgilio, Francesco Fuso, Umberto Giacomelli, et al. Constraining theories of gravity by ginger experiment. *The European Physical Journal Plus*, 136(4):1–21, 2021.
- [26] CW Francis Everitt, DB DeBra, BW Parkinson, JP Turneare, JW Conklin, MI Heifetz, GM Keiser, AS Silbergleit, T Holmes, J Kolodziejczak, et al. Gravity probe B: final results of a space experiment to test general relativity. *Physical Review Letters*, 106(22):221101, 2011.
- [27] Ignazio Ciufolini and Erricos C Pavlis. A confirmation of the general relativistic prediction of the lense–thirring effect. *Nature*, 431(7011):958–960, 2004.
- [28] Sylvester Lacour, FH Vincent, M Nowak, A Le Tiec, V Lapeyriere, L David, P Bourget, A Kellerer, K Jani, J Martino, et al. Sage: finding imbh in the black hole desert. *Classical and Quantum Gravity*, 36(19):195005, 2019.
- [29] Heonoh Kim, Osung Kwon, and Han Seb Moon. Pulsed sagnac source of polarization-entangled photon pairs in telecommunication band. *Scientific reports*, 9(1):1–7, 2019.
- [30] Youn Seok Lee, Mengyu Xie, Ramy Tannous, and Thomas Jennewein. Sagnac-type entangled photon source using only conventional polarization optics. *Quantum Science and Technology*, 6(2):025004, 2021.
- [31] Ivette Fuentes-Schuller and Robert B Mann. Alice falls into a black hole: entanglement in noninertial frames. *Physical Review Letters*, 95(12):120404, 2005.
- [32] Paul M Alsing and Ivette Fuentes. Observer-dependent entanglement. *Classical and Quantum Gravity*, 29(22):224001, 2012.
- [33] Georges Sagnac. L'éther lumineux démontré par l'effet du vent relatif d'éther dans un interféromètre en rotation uniforme. *CR Acad. Sci.*, 157:708–710, 1913.
- [34] Georges Sagnac. Sur la preuve de la réalité de l'éther lumineux par l'expérience de l'interféromètre tournant. *CR Acad. Sci.*, 157:1410–1413, 1913.
- [35] Albert Einstein. Letter to Sommerfeld. *Albert Einstein-Arnold Sommerfeld. Briefwechsel. Armin Hermann, ed. Basel and Stuttgart*, 1909.
- [36] Jan Ivar Korsbakken and Jon Magne Leinaas. Fulling-Unruh effect in general stationary accelerated frames. *Physical Review D*, 70(8):084016, 2004.
- [37] Miles J Padgett. On diffraction within a dielectric medium as an example of the Minkowski formulation of optical momentum. *Optics Express*, 16(25):20864–20868, 2008.
- [38] Stephen M Barnett. Resolution of the abraham-minkowski dilemma. *Physical Review Letters*, 104(7):070401, 2010.
- [39] Evert Jan Post. Sagnac effect. *Reviews of Modern Physics*, 39(2):475, 1967.
- [40] Ronald Anderson, HR Bilger, and GE Stedman. "Sagnac" effect: A century of earth-rotated interferometers. *American Journal of Physics*, 62(11):975–985, 1994.
- [41] Grigori B Malykin. The sagnac effect: correct and incorrect explanations. *Physics-Uspekhi*, 43(12):1229, 2000.
- [42] Kip S Thorne, Charles W Misner, and John Archibald Wheeler. *Gravitation*. Freeman San Francisco, CA, 2000.
- [43] David A Vallado. *Fundamentals of astrodynamics and applications*, volume 12. Springer Science & Business Media, 2001.
- [44] Yakir Aharonov and Tirzah Kaufherr. Quantum frames of reference. *Physical Review D*, 30(2):368, 1984.
- [45] Flaminia Giacomini, Esteban Castro-Ruiz, and Časlav Brukner. Relativistic quantum reference frames: the operational meaning of spin. *Physical review letters*, 123(9):090404, 2019.
- [46] Yoon-Ho Kim. Single-photon two-qubit entangled states: Preparation and measurement. *Physical Review A*, 67(4):040301, 2003.
- [47] Scott Hill and William K Wootters. Entanglement of a pair of quantum bits. *Physical review letters*, 78(26):5022, 1997.
- [48] Berthold-Georg Englert, Christian Kurtsiefer, and Harald Weinfurter. Universal unitary gate for single-photon two-qubit states. *Physical Review A*, 63(3):032303, 2001.
- [49] Otfried Gühne and Géza Tóth. Entanglement detection. *Physics Reports*, 474(1-6):1–75, 2009.
- [50] S Adhikari, AS Majumdar, Dipankar Home, and AK Pan. Swapping path-spin intraparticle entanglement onto spin-spin interparticle entanglement. *EPL (Europhysics Letters)*, 89(1):10005, 2010.
- [51] Asmita Kumari, Abhishek Ghosh, Mohit Lal Bera, and AK Pan. Swapping intraphoton entanglement to interphoton entanglement using linear optical devices. *Physical Review A*, 99(3):032118, 2019.
- [52] Zihao Chen, Yao Zhou, and Jung-Tsung Shen. Photon antibunching and bunching in a ring-resonator waveguide quantum electrodynamics system. *Optics letters*, 41(14):3313–3316, 2016.
- [53] Zihao Chen, Yao Zhou, and Jung-Tsung Shen. Dissipation-induced photonic-correlation transition in waveguide-qed systems. *Physical Review A*, 96(5):053805, 2017.
- [54] Zihao Chen, Yao Zhou, Jung-Tsung Shen, Pei-Cheng Ku, and Duncan Steel. Two-photon controlled-phase gates enabled by photonic dimers. *Physical Review A*, 103(5):052610, 2021.
- [55] Magdalena Zych, Fabio Costa, Igor Pikovski, Timothy C Ralph, and Časlav Brukner. General relativistic effects in quantum interference of photons. *Classical and Quantum Gravity*, 29(22):224010, 2012.
- [56] Sougato Bose, Anupam Mazumdar, Gavin W Morley, Hendrik Ulbricht, Marko Toroš, Mauro Paternostro, Andrew A Geraci, Peter F Barker, MS Kim, and Gerard Milburn. Spin entanglement witness for quantum gravity. *Physical review letters*, 119(24):240401, 2017.
- [57] Chiara Marletto and Vlatko Vedral. Gravitationally induced entanglement between two massive particles is sufficient evidence of quantum effects in gravity. *Physical review letters*, 119(24):240402, 2017.
- [58] Ryan J Marshman, Anupam Mazumdar, and Sougato Bose. Locality and entanglement in table-top testing of the quantum nature of linearized gravity. *Physical Review A*, 101(5):052110, 2020.
- [59] Daine L Danielson, Gautam Satishchandran, and Robert M Wald. Gravitationally mediated entanglement: Newtonian field versus gravitons. *Physical Review D*, 105(8):086001, 2022.
- [60] Sougato Bose, Anupam Mazumdar, Martine Schut, and

- Marko Toroš. Mechanism for the quantum natured gravitons to entangle masses. *Phys. Rev. D*, 105:106028, May 2022.
- [61] Marios Christodoulou, Andrea Di Biagio, Markus Aspelmeyer, Časlav Brukner, Carlo Rovelli, and Richard Howl. Locally mediated entanglement through gravity from first principles. *arXiv preprint arXiv:2202.03368*, 2022.
- [62] Giovanni Amelino-Camelia. Quantum-spacetime phenomenology. *Living Reviews in Relativity*, 16(1):1–137, 2013.
- [63] Aaron Chou, Henry Glass, H Richard Gustafson, Craig J Hogan, Brittany L Kamai, Ohkyung Kwon, Robert Lanza, Lee McCuller, Stephan S Meyer, Jonathan W Richardson, et al. Interferometric constraints on quantum geometrical shear noise correlations. *Classical and Quantum Gravity*, 34(16):165005, 2017.
- [64] Sander M Vermeulen, Lorenzo Aiello, Aldo Ejlli, William L Griffiths, Alasdair L James, Katherine L Dooley, and Hartmut Grote. An experiment for observing quantum gravity phenomena using twin tabletop 3d interferometers. *Classical and Quantum Gravity*, 38(8):085008, 2021.
- [65] Erik P Verlinde and Kathryn M Zurek. Observational signatures of quantum gravity in interferometers. *Physics Letters B*, 822:136663, 2021.
- [66] Igor Pikovski, Michael R Vanner, Markus Aspelmeyer, MS Kim, and Časlav Brukner. Probing Planck-scale physics with quantum optics. *Nature Physics*, 8(5):393–397, 2012.
- [67] Giovanni Amelino-Camelia, John Ellis, NE Mavromatos, Dimitri V Nanopoulos, and Subir Sarkar. Tests of quantum gravity from observations of γ -ray bursts. *Nature*, 393(6687):763–765, 1998.
- [68] V Alan Kostelecký and Neil Russell. Data tables for lorentz and c p t violation. *Reviews of Modern Physics*, 83(1):11, 2011.
- [69] David Mattingly. Modern tests of lorentz invariance. *Living Reviews in Relativity*, 8(1):1–84, 2005.
- [70] Roger Penrose. On gravity’s role in quantum state reduction. *General relativity and gravitation*, 28(5):581–600, 1996.
- [71] Sandro Donadi, Kristian Piscicchia, Catalina Curceanu, Lajos Diósi, Matthias Laubenstein, and Angelo Bassi. Underground test of gravity-related wave function collapse. *Nature Physics*, 17(1):74–78, 2021.
- [72] I. J. Arnquist, F. T. Avignone, A. S. Barabash, C. J. Barton, K. H. Bhimani, E. Blalock, B. Bos, M. Busch, M. Buuck, T. S. Caldwell, Y-D. Chan, C. D. Christoferson, P.-H. Chu, M. L. Clark, C. Cuesta, J. A. Detwiler, Yu. Efremenko, H. Ejiri, S. R. Elliott, G. K. Giovanetti, M. P. Green, J. Gruszko, I. S. Guinn, V. E. Guiseppe, C. R. Haufe, R. Henning, D. Hervas Aguilar, E. W. Hoppe, A. Hostiuc, I. Kim, R. T. Kouzes, T. E. Lannen V., A. Li, A. M. Lopez, J. M. López-Castaño, E. L. Martin, R. D. Martin, R. Massarczyk, S. J. Meijer, T. K. Oli, G. Othman, L. S. Paudel, W. Pettus, A. W. P. Poon, D. C. Radford, A. L. Reine, K. Rielage, N. W. Ruof, D. Tedeschi, R. L. Varner, S. Vasilyev, J. F. Wilkerson, C. Wiseman, W. Xu, C.-H. Yu, and B. X. Zhu. Search for spontaneous radiation from wave function collapse in the majorana demonstrator. *Phys. Rev. Lett.*, 129:080401, Aug 2022.
- [73] Angelo Bassi, André Großardt, and Hendrik Ulbricht. Gravitational decoherence. *Classical and Quantum Gravity*, 34(19):193002, 2017.
- [74] Albert Abraham Michelson. The Effect of the Earth’s Rotation on the Velocity of Light, i. *The Astrophysical Journal*, 61:137, 1925.
- [75] Albert Abraham Michelson and Henry G Gale. The Effect of the Earth’s Rotation on the Velocity of Light, ii. *The Astrophysical Journal*, 61:140, 1925.
- [76] Hans-A Bacher and Timothy C Ralph. *A guide to experiments in quantum optics*. John Wiley & Sons, 2019.

Supplemental material

A. Initial state preparation and basic definitions

We suppose we have the prepared the photon state:

$$|\psi_{\text{source}}\rangle = (1, 0, 0, 0)^\top, \quad (\text{S1})$$

corresponding to the photon on a single path and polarization $|H\rangle$. The state in Eq. (S1) is a two-qubit state in $\mathcal{H}_{\mathcal{P}} \otimes \mathcal{H}_{\Pi}$, where $\mathcal{H}_{\mathcal{P}}$ (\mathcal{H}_{Π}) denote the path (polarization) Hilbert space. Such a state can be prepared using a photon source and optical elements (see for example [76]). Let us now see how the optical elements shown in Fig. 1(a) transform the state in Eq. (S1) to the initial state defined in Eq. (3).

We first recall the quarter-wave plate (QWP) and half-wave plate (HWP) matrix transformations:

$$U_{\text{QWP}}(\theta) = \frac{1}{\sqrt{2}} \begin{bmatrix} 1 - i \cos(2\theta) & -i \sin(2\theta) \\ -i \sin(2\theta) & 1 + i \cos(2\theta) \end{bmatrix}, \quad (\text{S2})$$

$$U_{\text{HWP}}(\theta) = -i \begin{bmatrix} \cos(2\theta) & \sin(2\theta) \\ \sin(2\theta) & -\cos(2\theta) \end{bmatrix}, \quad (\text{S3})$$

respectively, where θ denotes the angle of rotation.

The first half-wave plate shown Fig. 1(a) is described by the matrix transformation

$$U_{\text{HWP1}} = \begin{bmatrix} U_{\text{HWP}}(\pi/8) & 0 \\ 0 & 1 \end{bmatrix}. \quad (\text{S4})$$

We then construct the transformation matrix for a polarizing beam splitter (PBS), where the basis vectors are given by:

$$|aH\rangle = \frac{1}{\sqrt{2}}(1, 0, 0, 0)^\top, \quad (\text{S5})$$

$$|aV\rangle = \frac{1}{\sqrt{2}}(0, 1, 0, 0)^\top, \quad (\text{S6})$$

$$|bH\rangle = \frac{1}{\sqrt{2}}(0, 0, 1, 0)^\top, \quad (\text{S7})$$

$$|bV\rangle = \frac{1}{\sqrt{2}}(0, 0, 0, 1)^\top. \quad (\text{S8})$$

We define the PBS transformation as

$$U_{\text{PBS}} = |aH\rangle\langle aH| + |bH\rangle\langle bH| + |aV\rangle\langle bV| + |bV\rangle\langle aV|, \quad (\text{S9})$$

which gives the following transformation matrix

$$U_{\text{PBS}} = \frac{1}{2} \begin{bmatrix} 1 & 0 & 0 & 0 \\ 0 & 0 & 0 & 1 \\ 0 & 0 & 1 & 0 \\ 0 & 1 & 0 & 0 \end{bmatrix}. \quad (\text{S10})$$

Finally, the two HWPs after the PBS corresponds to the following matrix transformation

$$U_{\text{HWP2}} = \begin{bmatrix} U_{\text{HWP}}(\pi/8) & 0 \\ 0 & U_{\text{HWP}}(3\pi/8) \end{bmatrix}. \quad (\text{S11})$$

Applying the transformations in Eqs. (S4), (S10) and (S11) to the state in Eq. (S1) we readily find

$$|\psi_{\text{initial}}\rangle = U_{\text{HWP2}} U_{\text{PBS}} U_{\text{HWP1}} |\psi_{\text{source}}\rangle \quad (\text{S12})$$

$$= \frac{1}{2}(1, 1, 1, 1)^\top, \quad (\text{S13})$$

which is the state given in Eq. (3), written in vector form.

B. Bell state basis

The state obtained in Eq. (4) can be written in vector form as

$$|\psi_{\text{final}}\rangle = \frac{1}{2}(e^{-\frac{i\Omega r_a p t}{\hbar}}, e^{+\frac{i\Omega r_a p t}{\hbar}}, e^{-\frac{i\Omega r_b p t}{\hbar}}, e^{+\frac{i\Omega r_b p t}{\hbar}})^\top. \quad (\text{S14})$$

The state $|\psi_{\text{final}}\rangle$ can become maximally entangled when the rotational frequency Ω reaches any odd multiple of Ω_{Bell} defined in Eq. (9). Specifically, we obtain the Bell states in Eqs. (10) and (11) which can be written in vector form as

$$|\psi_1\rangle = \frac{1}{2}(e^{-i\frac{\pi}{2}\delta r_a}, e^{i\frac{\pi}{2}\delta r_a}, e^{-i\frac{\pi}{2}\delta r_b}, e^{i\frac{\pi}{2}\delta r_b})^\top, \quad (\text{S15})$$

$$|\psi_2\rangle = \frac{1}{2}(e^{-i\frac{3\pi}{2}\delta r_a}, e^{i\frac{3\pi}{2}\delta r_a}, e^{-i\frac{3\pi}{2}\delta r_b}, e^{i\frac{3\pi}{2}\delta r_b})^\top, \quad (\text{S16})$$

with $\delta r_j = r_j/\Delta r$ ($j = a, b$). Following the main text, we choose for simplicity $r_b = 2r_a$ (such that $\Delta r = r_b - r_a = r_a = r_b/2$ and $\delta r_a = \delta r_b/2 = 1$), which transforms the states in Eqs. (S15) and (S16) to

$$|\psi_1\rangle = \frac{1}{2}(-i, i, -1, -1)^\top, \quad (\text{S17})$$

$$|\psi_2\rangle = \frac{1}{2}(i, -i, -1, -1)^\top. \quad (\text{S18})$$

Furthermore, we introduce two additional states

$$|\psi_3\rangle = \frac{1}{2}(-1, -1, -i, i)^\top, \quad (\text{S19})$$

$$|\psi_4\rangle = \frac{1}{2}(-1, -1, i, -i)^\top. \quad (\text{S20})$$

In this way the states $|\psi_j\rangle$ ($j = 1, \dots, 4$) form an orthonormal basis of $\mathcal{H}_{\mathcal{P}} \otimes \mathcal{H}_{\Pi}$.

We can readily verify that the states $|\psi_j\rangle$ ($j = 1, \dots, 4$) are maximally entangled by computing the concurrence [47]

$$C = 2|\mathbf{a}_1\mathbf{a}_4 - \mathbf{a}_2\mathbf{a}_3|, \quad (\text{S21})$$

where $\mathbf{a}_1, \dots, \mathbf{a}_4$ denote the components of the vector in Eq. (S14). For the states $|\psi_j\rangle$ ($j = 1, \dots, 4$) we find the value $C = 1$ which is the maximum possible value for any entangled state on $\mathcal{H}_{\mathcal{P}} \otimes \mathcal{H}_{\Pi}$.

C. Bell state projection scheme

The Bell states defined in Eqs. (S17)-(S20) can be measured using the scheme shown in Fig. 1(b) [46]. The scheme consists of a polarizing beam splitter (PBS) at 45° and quarter-wave plates (QWPs) at angle 45° .

We first construct the transformation matrix for a polarizing beam splitters (PBS) at 45° . The basis vectors are given by:

$$|aD\rangle = \frac{1}{\sqrt{2}}(1, 1, 0, 0)^\top, \quad (\text{S22})$$

$$|aA\rangle = \frac{1}{\sqrt{2}}(1, -1, 0, 0)^\top, \quad (\text{S23})$$

$$|bD\rangle = \frac{1}{\sqrt{2}}(0, 0, 1, 1)^\top, \quad (\text{S24})$$

$$|bA\rangle = \frac{1}{\sqrt{2}}(0, 0, 1, -1)^\top. \quad (\text{S25})$$

We can then define the transformation of the PBS at 45° as

$$U_{\text{PBS}}(\pi/4) = |aD\rangle\langle aD| + |bD\rangle\langle bD| + |aA\rangle\langle bA| + |bA\rangle\langle aA|, \quad (\text{S26})$$

which gives the following transformation matrix

$$U_{\text{PBS}}(\pi/4) = \frac{1}{2} \begin{bmatrix} 1 & 1 & 1 & -1 \\ 1 & 1 & -1 & 1 \\ 1 & -1 & 1 & 1 \\ -1 & 1 & 1 & 1 \end{bmatrix}. \quad (\text{S27})$$

The QWP at angle 45° is defined by the following transformation matrix (see Eq. (S2) for the general definition)

$$U_{\text{QWP}}(\pi/4) \equiv \frac{e^{-i\pi/4}}{2} \begin{pmatrix} 1+i & 1-i \\ 1-i & 1+i \end{pmatrix}. \quad (\text{S28})$$

We can now define the transformation corresponding to the scheme in Fig. 1(b) as

$$\mathcal{U}_{\mathcal{B}} = \begin{bmatrix} U_{\text{QWP}}(\pi/4) & 0 \\ 0 & U_{\text{QWP}}(\pi/4) \end{bmatrix} U_{\text{PBS}}(\pi/4). \quad (\text{S29})$$

We find

$$\mathcal{U}_{\mathcal{B}}|\psi_1\rangle = -e^{-i\pi/4}(0, 0, 0, 1)^\top, \quad (\text{S30})$$

$$\mathcal{U}_{\mathcal{B}}|\psi_2\rangle = -e^{-i\pi/4}(0, 0, 1, 0)^\top, \quad (\text{S31})$$

$$\mathcal{U}_{\mathcal{B}}|\psi_3\rangle = -e^{-i\pi/4}(0, 1, 0, 0)^\top, \quad (\text{S32})$$

$$\mathcal{U}_{\mathcal{B}}|\psi_4\rangle = -e^{-i\pi/4}(1, 0, 0, 0)^\top, \quad (\text{S33})$$

where the global phase factors are not important here. The four detectors B_1, \dots, B_4 in Fig. 1(b) will thus give a maximum signal whenever we are in one of the Bell state $|\psi_1\rangle, \dots, |\psi_4\rangle$, respectively, while the other three detectors will show a null signal. In our specific experimental configuration we see that the detectors B_1 and B_2 can thus identify the two Bell states $|\psi_1\rangle$ and $|\psi_2\rangle$, respectively (see Fig. 1(c)).

D. Construction of optimal entanglement witness

To assert the generated entanglement using the scheme in Fig. 1, we construct an optimal entanglement witness [49].

We consider first the Bell state $|\psi_1\rangle$ defined in Eq. (S54), where we have assumed for simplicity $\Delta r = r_b - r_a = r_a = r_b/2$ and $\delta r_a = \delta r_b/2 = 1$ following the main text. In order to estimate the robustness of the witness that we are going to identify, we introduce the Werner state

$$\rho[p] = p|\psi_1\rangle\langle\psi_1| + \frac{(1-p)}{4}\mathbb{I}_4, \quad (\text{S34})$$

where p is the probability of preparing the desired state and \mathbb{I}_n is a $n \times n$ identity matrix. The first (second) term on the right-hand side of Eq. (S34) denotes the contributions from the ideal entangled state (a mixed non-entangled state which could arise from any number of noise or decoherence sources and is typically referred to as *white noise*). Provided the probability of preparing the desired states satisfies the condition $p > 1/3$, the partially transposed density matrix would have the negative eigenvalue $(1-3p)/4$, with the associated eigenstate $|\phi_m\rangle = \frac{1}{2}(i, i, -1, 1)^\top$, thus affirming entanglement in light of the Peres-Horodecki criterion. One can then readily construct the optimal fidelity-based entanglement witness $\mathcal{W} \equiv |\phi_m\rangle\langle\phi_m|^{\text{Tn}}$, which reduces to

$$\mathcal{W}_1 = \frac{1}{4} \begin{bmatrix} 1 & 1 & -i & -i \\ 1 & 1 & i & i \\ i & -i & 1 & -1 \\ i & -i & -1 & 1 \end{bmatrix}. \quad (\text{S35})$$

One can then show that the witness in Eq. (S35) can be decomposed in the following set of local operations

$$\mathcal{W}_1 = \frac{1}{4} [\mathbb{I}_4 + \sigma_x^{\mathcal{P}} \sigma_y^{\Pi} + \sigma_y^{\mathcal{P}} \sigma_z^{\Pi} + \sigma_z^{\mathcal{P}} \sigma_x^{\Pi}], \quad (\text{S36})$$

where $\sigma_k^{\mathcal{J}}$ denotes the $k = x, y, z$ Pauli operator for $\mathcal{J} = \mathcal{P}, \Pi$.

A similar calculation can be performed for the other maximally entangled state $|\psi_2\rangle$ in Eq. (S18). Specifically, following the steps in Eqs. (S15)-(S35) we find the witness

$$\mathcal{W}_2 = \frac{1}{4} [\mathbb{I}_4 - \sigma_x^{\mathcal{P}} \sigma_y^{\Pi} - \sigma_y^{\mathcal{P}} \sigma_z^{\Pi} + \sigma_z^{\mathcal{P}} \sigma_x^{\Pi}]. \quad (\text{S37})$$

Therefore, the set of local operations needed to reconstruct the value of \mathcal{W}_1 and \mathcal{W}_2 is the same.

E. Measuring entanglement witnesses using the universal unitary gate

The entanglement witnesses in Eqs. (S36) and (S37) can be implemented using the universal unitary gate for single-photon two-qubit states shown in Fig. 1(d) [48]. Such a gate can be used to perform a measurement of a generic 2-qubit observable \mathcal{O} using linear optical elements.

1. Constructing the gate

We first summarize how to construct the unitary gate given a 2-qubit observable \mathcal{O} . We first find the eigenvectors of the observable \mathcal{O} which we denote by $|e_j\rangle$ ($j = 1, \dots, 4$) and then construct the operators

$$A = |e_1\rangle\langle e_1| + |e_2\rangle\langle e_2| - |e_3\rangle\langle e_3| - |e_4\rangle\langle e_4|, \quad (\text{S38})$$

$$B = |e_1\rangle\langle e_1| - |e_2\rangle\langle e_2| + |e_3\rangle\langle e_3| - |e_4\rangle\langle e_4|. \quad (\text{S39})$$

The gate S is then defined as the transformations that achieves

$$SAS^\dagger = \sigma_z^{\mathcal{P}}, \quad SBS^\dagger = \sigma_z^{\Pi}. \quad (\text{S40})$$

The measurement of the path observable $\sigma_z^{\mathcal{P}}$ distinguishes between $|e_1\rangle, |e_2\rangle$ (eigenvalue +1) and $|e_3\rangle, |e_4\rangle$ (eigenvalue -1), while the measurement of the polarization observable σ_z^{Π} selects between $|e_1\rangle, |e_3\rangle$ (eigenvalue +1) and $|e_2\rangle, |e_4\rangle$ (eigenvalue -1) – the two measurements together thus uniquely identify the eigenstate. Hence the transformation S maps eigenstates of \mathcal{O} to the output ports where they are measured by the detectors D_j ($j = 1, \dots, 4$) shown in Fig. 1(d). In this sense the universal unitary gate can be seen as a generalization of the (simpler) Bell state projection gate discussed in Sec. C.

The gate S can be conveniently written in component form as

$$S = \begin{bmatrix} S_{RR} & S_{RL} \\ S_{LR} & S_{LL} \end{bmatrix}, \quad (\text{S41})$$

where the 2×2 matrix acts on $\mathcal{H}^{\mathcal{P}}$, and the matrices $S_{RR}, S_{LL}, S_{RL}, S_{LR}$ on the polarization Hilbert space \mathcal{H}^{Π} . We recall that the entanglement witnesses \mathcal{W}_1 and \mathcal{W}_2 defined in Eqs. (S36) and (S37) are composed by three observables: $\sigma_x^{\mathcal{P}} \sigma_y^{\Pi}, \sigma_y^{\mathcal{P}} \sigma_z^{\Pi}$ and $\sigma_z^{\mathcal{P}} \sigma_x^{\Pi}$. We list the components of the matrix S for each of these observables in Table. I.

2. Implementing the gate

The universal gate shown Fig. 1(d) consists of two beam-splitters (BSs), which together with the mirrors forms a Mach-Zehnder interferometer, and of four composite optical elements denoted by V_j ($j = 1, 2, R, L$). Each element V_j is composed of a half-wave plate (HWP) inserted between two quarter-wave plates (QWPs) and an additional phase shifter. The associated unitary transformation is given by

$$V_j = e^{i\delta} U_{\text{QWP}}(\gamma) U_{\text{HWP}}(\beta) U_{\text{QWP}}(\alpha), \quad (\text{S42})$$

where δ is a phase shift, and α, β, γ denote the first QWP, middle HWP, and second QWP angle, respectively. The QWP and HWP transformations matrices are given in Eqs. (S2) and (S3), respectively.

Let us summarize the procedure for choosing the angles $\alpha, \beta, \gamma, \delta$ that will realize the gates S obtained in Table. I (and hence the measurement of the corresponding observables \mathcal{O}). The first step is to decompose the matrix S exploiting its unitary character. In particular, it has been shown that the matrix S can be rewritten in the following way:

$$S_{RR} = \cos(\theta_1) |\bar{\psi}_1\rangle\langle\psi_1| + \cos(\theta_2) |\bar{\psi}_2\rangle\langle\psi_2|, \quad (\text{S43})$$

$$S_{LL} = \cos(\theta_1) |\bar{\chi}_1\rangle\langle\chi_1| + \cos(\theta_2) |\bar{\chi}_2\rangle\langle\chi_2|, \quad (\text{S44})$$

$$S_{RL} = -i(\sin(\theta_1) |\bar{\psi}_1\rangle\langle\chi_1| + \sin(\theta_2) |\bar{\psi}_2\rangle\langle\chi_2|), \quad (\text{S45})$$

$$S_{LR} = -i(\sin(\theta_1) |\bar{\chi}_1\rangle\langle\psi_1| + \sin(\theta_2) |\bar{\chi}_2\rangle\langle\psi_2|). \quad (\text{S46})$$

The left-hand side of Eqs. (S43)-(S46) are listed in Table I and we can determine the angles and vectors appearing on the right-hand side in the following way. From $S_{RR}^\dagger S_{RR}$ we first obtain the eigenvectors $|\psi_j\rangle$ ($j = 1, 2$) as well as the angles θ_j ($j = 1, 2$), up to arbitrary phases. From $S_{RR}^\dagger S_{RR}^\dagger, S_{LL}^\dagger S_{LL}$, and $S_{LL}^\dagger S_{LL}^\dagger$ we then determine the eigenvectors $|\psi_j\rangle, |\chi_j\rangle$, and $|\bar{\chi}_j\rangle$, respectively. Using the decomposition in Eqs. (S43)-(S46) we then construct the four transformation matrices:

$$V_1 = -i|\chi_1\rangle\langle\psi_1| - i|\chi_2\rangle\langle\psi_2|, \quad (\text{S47})$$

$$V_2 = i|\bar{\psi}_1\rangle\langle\bar{\chi}_1| + i|\bar{\psi}_2\rangle\langle\bar{\chi}_2|, \quad (\text{S48})$$

$$V_R = e^{-i\theta_1} |\bar{\chi}_1\rangle\langle\chi_1| + e^{-i\theta_2} |\bar{\chi}_2\rangle\langle\chi_2|, \quad (\text{S49})$$

$$V_L = e^{i\theta_1} |\bar{\chi}_1\rangle\langle\chi_1| + e^{i\theta_2} |\bar{\chi}_2\rangle\langle\chi_2|. \quad (\text{S50})$$

| \mathcal{O} | S_{RR} | S_{LL} | S_{RL} | S_{LR} |
|---|---|--|--|--|
| $\sigma_x^{\mathcal{P}} \sigma_y^{\Pi}$ | $\frac{1}{\sqrt{2}} \sigma_z^{\Pi}$ | $\frac{1}{\sqrt{2}} \sigma_x^{\Pi}$ | $-\frac{i}{\sqrt{2}} \sigma_x^{\Pi}$ | $-\frac{i}{\sqrt{2}} \sigma_z^{\Pi}$ |
| $\sigma_y^{\mathcal{P}} \sigma_z^{\Pi}$ | $\frac{1}{\sqrt{2}} \sigma_x^{\Pi}$ | $\frac{1+i}{2\sqrt{2}} (\sigma_x^{\Pi} + \sigma_y^{\Pi})$ | $-\frac{1}{\sqrt{2}} \sigma_y^{\Pi}$ | $\frac{1+i}{2\sqrt{2}} (\sigma_x^{\Pi} - \sigma_y^{\Pi})$ |
| $\sigma_z^{\mathcal{P}} \sigma_x^{\Pi}$ | $\frac{1}{2\sqrt{2}} (-\mathbb{I}^{\Pi} + \sigma_x^{\Pi} - i\sigma_y^{\Pi} + \sigma_z^{\Pi})$ | $\frac{1}{2\sqrt{2}} (\mathbb{I}^{\Pi} - \sigma_x^{\Pi} - i\sigma_y^{\Pi} + \sigma_z^{\Pi})$ | $\frac{1}{2\sqrt{2}} (\mathbb{I}^{\Pi} + \sigma_x^{\Pi} + i\sigma_y^{\Pi} + \sigma_z^{\Pi})$ | $\frac{1}{2\sqrt{2}} (\mathbb{I}^{\Pi} + \sigma_x^{\Pi} - i\sigma_y^{\Pi} - \sigma_z^{\Pi})$ |

Table I. Components of the unitary 2-qubit gate defined in Eq. (S41) which maps the four eigenstates of the 2-qubit observable \mathcal{O} to the four output ports D_j ($j = 1, \dots, 4$) shown in Fig. 1(d).

| \mathcal{O} | V_1 | α | β | γ | δ | V_L | α | β | γ | δ | V_R | α | β | γ | δ | V_2 | α | β | γ | δ |
|---|--------------------|----------|-----------------|-----------------|-----------------|--|------------------|------------------|-----------------|------------------|---|------------------|------------------|------------------|-------------------|---|------------------|------------------|------------------|------------------|
| $\sigma_x^{\mathcal{P}} \sigma_y^{\Pi}$ | $-\sigma_y^{\Pi}$ | 0 | $\frac{\pi}{4}$ | $\frac{\pi}{2}$ | $\frac{\pi}{2}$ | $e^{i\frac{\pi}{4}} \sigma_x^{\Pi}$ | 0 | $\frac{\pi}{4}$ | 0 | $\frac{3\pi}{4}$ | $e^{-i\frac{\pi}{4}} \sigma_x^{\Pi}$ | $\frac{\pi}{4}$ | $-\frac{\pi}{4}$ | $-\frac{\pi}{4}$ | $-\frac{3\pi}{4}$ | $i\mathbb{I}^{\Pi}$ | $\frac{\pi}{4}$ | 0 | $\frac{\pi}{4}$ | π |
| $\sigma_y^{\mathcal{P}} \sigma_z^{\Pi}$ | $-i\sigma_z^{\Pi}$ | 0 | 0 | $\frac{\pi}{2}$ | 0 | $\frac{i}{\sqrt{2}} (\sigma_x^{\Pi} + \sigma_y^{\Pi})$ | $-\frac{\pi}{4}$ | $\frac{3\pi}{8}$ | $\frac{\pi}{4}$ | $-\pi$ | $\frac{1}{\sqrt{2}} (\sigma_x^{\Pi} + \sigma_y^{\Pi})$ | $-\frac{\pi}{4}$ | $-\frac{\pi}{8}$ | $\frac{\pi}{4}$ | $-\frac{\pi}{2}$ | $\frac{1-i}{2} \mathbb{I}^{\Pi} - \frac{1+i}{2} \sigma_z^{\Pi}$ | $-\frac{\pi}{4}$ | $\frac{\pi}{8}$ | $-\frac{\pi}{4}$ | $-\frac{\pi}{4}$ |
| $\sigma_z^{\mathcal{P}} \sigma_x^{\Pi}$ | $-i\sigma_z^{\Pi}$ | 0 | 0 | 0 | $\frac{\pi}{2}$ | $\frac{1}{\sqrt{2}} (\sigma_z^{\Pi} - \sigma_x^{\Pi})$ | 0 | $-\frac{\pi}{8}$ | $\frac{\pi}{4}$ | $\frac{\pi}{2}$ | $\frac{1}{\sqrt{2}} (\mathbb{I}^{\Pi} - i\sigma_y^{\Pi})$ | 0 | $\frac{\pi}{8}$ | $\frac{\pi}{4}$ | π | $i\sigma_x^{\Pi}$ | 0 | $-\frac{\pi}{4}$ | 0 | 0 |

Table II. Configuration of the angles of the HWP, QWPs, and phase shifter to measure the entanglement witnesses defined in Eqs. (S36) and (S37).

The matrices V_j ($j = 1, 2, R, L$) are then finally decomposed in the form of Eq. S42 by a suitable choice of the angles $\alpha, \beta, \gamma, \delta$. The matrices V_j ($j = 1, 2, R, L$) together with the angles $\alpha, \beta, \gamma, \delta$ are listed in Table. II.

F. Alternative single loop scheme

We present an alternative implementation of the platform illustrated in the main text of the paper. Specifically, we demonstrate that entangled path-polarization states akin to those discussed in the main text of the paper can be readily generated through a single-loop scheme. To this end, we send the photon into four different paths as shown in Fig. S1. The corresponding four states $|a\rangle|H\rangle, |a\rangle|V\rangle, |b\rangle|H\rangle, |b\rangle|V\rangle$ acquire Sagnac phases. Specifically, from the coupling $\sim rp$ in Eq. (1) we find that the phases are given by $\phi_{\pm} = \pm\Omega r p t / \hbar$, where $t = \frac{nl}{c}$ is the the flight time, n is the refractive index of the fiber, $l = 2\pi r$ is the length of the fibers (automatically equal for the two paths), c is the speed of light, $p = E/(nc) = \hbar\omega/(nc)$ is the momentum, and ω is the mean photon frequency. We note that the phases can be rewritten as $\phi_{\pm} = \pm\Omega r p t / \hbar = \pm 2\Omega\omega\mathcal{A}/c^2$, where $\mathcal{A} = \pi r^2$ is the effective area of the interferometer. The phases $\phi_{\pm} = \pm\phi_s/2$ can be seen as variants of the Sagnac phase $\phi_s \equiv 4\Omega\omega\mathcal{A}/c^2$. Importantly, the phases ϕ_{\pm} do not depend on the refractive index of the medium which indicates that the effect is ultimately linked to the geometry of spacetime [15].

The initial (non-entangled) state is given by

$$|\psi_{\text{initial}}\rangle = \frac{1}{2}(|a\rangle + |b\rangle)(|H\rangle + |V\rangle), \quad (\text{S51})$$

and the final state is given by

$$|\psi_{\text{final}}\rangle = \frac{1}{2} \left(|a\rangle [e^{-i\frac{\phi_s}{2}} |H\rangle + e^{+i\frac{\phi_s}{2}} |V\rangle] + |b\rangle [e^{+i\frac{\phi_s}{2}} |H\rangle + e^{-i\frac{\phi_s}{2}} |V\rangle] \right), \quad (\text{S52})$$

where we have used the Hamiltonian H_{rot} defined in Eq. (1).

Let us consider first the case $\Omega = 0$. The final state in Eq. (S52) reduces to the initial state in Eq. (S51) and thus a non-rotating platform has no effect on entanglement. In contrast, when $\Omega \neq 0$ the state in Eq. (S52) will in general become entangled (as we can no longer write it as the product of the path and polarization states). This shows that non-inertial rotating motion generates entanglement.

Along the same lines as those presented in the main body of the paper, we look for the condition to achieve maximum entanglement, which is achieved when the polarization states in the square brackets of Eq. (S52) become orthogonal. Such condition is witnessed by the null overlap S of the polarization states. We readily find $S = \cos(\phi_s)$, so that the rotation frequency should achieve the value

$$\Omega_{\text{Bell}} \equiv \frac{(2k+1)\pi c^2}{8\omega\mathcal{A}} \quad (k \in \mathbb{Z}). \quad (\text{S53})$$

However, if we set the rotation frequency Ω to any odd multiple frequency of Ω_{Bell} we will also generate a maximally entangled Bell state. On the other hand, the resulting state would be separable for $\Omega = \pm 2n\Omega_{\text{Bell}}$ ($n \in \mathbb{Z}$). Therefore, similar considerations to those made in the main body of the paper in regard to the double-loop scheme can be put forward in this case as well. In particular, the scheme will generate the Bell-states

$$|\psi_1\rangle \sim |a\rangle[(1-i)|H\rangle + (1+i)|V\rangle] + |b\rangle[(1+i)|H\rangle + (1-i)|V\rangle] \quad (\text{S54})$$

at $\Omega/\Omega_{\text{Bell}} = \dots, -7, -3, 1, 5, \dots$, and

$$|\psi_2\rangle \sim |a\rangle[(-1-i)|H\rangle + (-1+i)|V\rangle] + |b\rangle[(-1+i)|H\rangle + (-1-i)|V\rangle] \quad (\text{S55})$$

at $\Omega/\Omega_{\text{Bell}} = \dots, -5, -1, 3, 7, \dots$

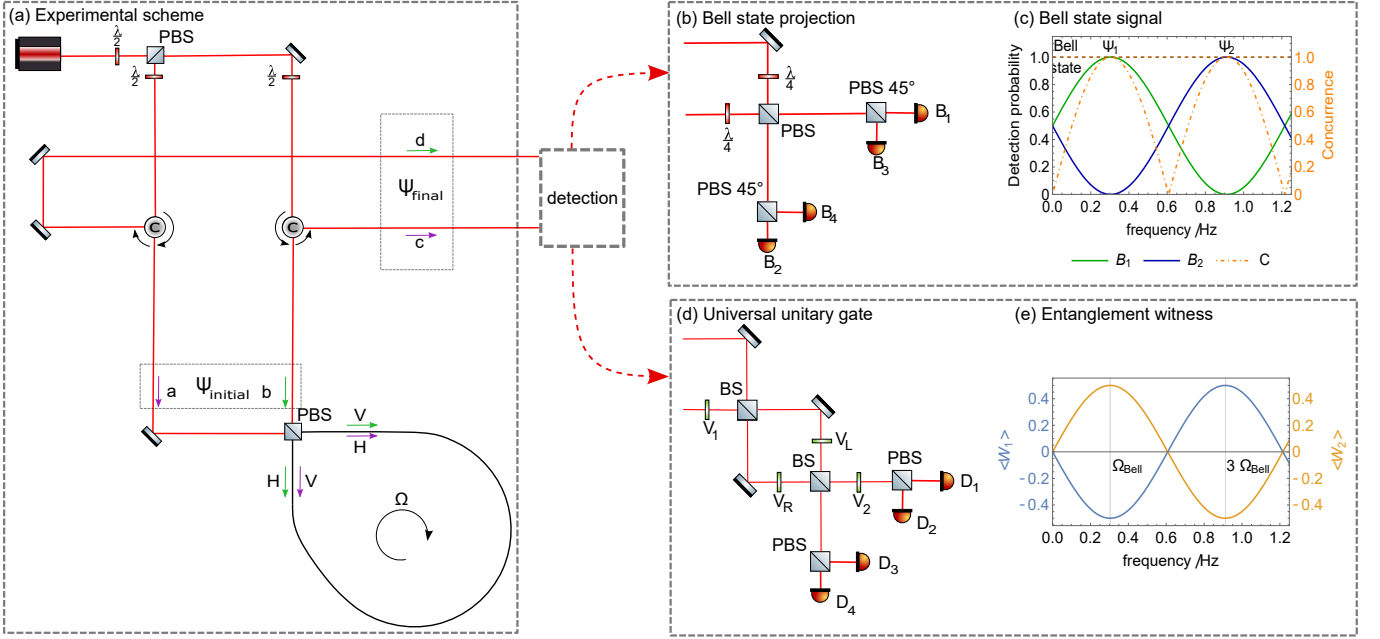


Figure S1. Single loop scheme for generating path-polarization entanglement from mechanical rotation. **(a)** The scheme consists of a single photon source, polarizing beam splitters (PBSs), and half-wave plates (HWPs) denoted by $\lambda/2$, and two optical circulators denoted by the letter C in a circle. We consider the same experimental values as in Fig. 1 of the main text (with the radius of the single loop set to $r = 0.5\text{m}$). The experimental setup is placed on a platform which can be set in rotation with frequency Ω . The purple and green arrows indicate the paths a, b , while the polarization is denoted by H, V . We start with a separable path-polarization photon $|\psi_{\text{initial}}\rangle$ – depending on the frequency of rotation Ω the final photon $|\psi_{\text{final}}\rangle$ can remain separable or become entangled. We can generate maximally entangled Bell states by tuning the frequency of the platform to $\Omega_{\text{Bell}} = \mathcal{N}\pi c^2 / (8\omega\mathcal{A})$, where ω is the mean photon frequency, and \mathcal{A} is the effective area of the interferometer (the path length assumed to be equal for the a, b paths), and $\mathcal{N} = 1, 3, 5, \dots$ **(b)** The detector B_j measures the Bell-state ψ_j ($j = 1, \dots, 4$). The first PBS is rotated by $\pi/4$, and the quarter-wave plates (QWPs) are denoted by $\lambda/4$ (with the fast axis oriented at $\pi/4$ which transforms circular polarization to linear polarization). **(c)** The detector B_1 (B_2) measures the maximally entangled Bell-state ψ_1 (ψ_2) at frequency Ω_{Bell} ($3\Omega_{\text{Bell}}$) where the concurrence achieves the maximum possible value $C = 1$. We find $\Omega_{\text{Bell}} \sim 2\pi \times 0.3\text{Hz}$, which can be readily achieved with similar photonic setups [14]. **(d)** Universal unitary gate for single-photon two-qubit states which can be used for tomographic reconstruction or implementing entanglement witnesses. The two beam-splitters (BSs) together with the mirrors form a Mach-Zehnder interferometer, and V_j ($j = 1, R, L, 2$) denotes an optical element composed of a HWP, two enclosing QWPs, and a phase shifter. **(e)** Optimal entanglement witnesses \mathcal{W}_1 (\mathcal{W}_2) for the maximally entangled Bell-state ψ_1 (ψ_2) as a function of rotation frequency. Entanglement is witnessed when $\mathcal{W}_j < 0$ ($j = 1, 2$).

We summarize below the details of the two detection schemes shown in Fig. S1(b)-S1(e) following the analysis performed for the double loop scheme in the Supplementary material B-E.

1. Bell state basis

We recast the two states in Eqs. (S54) and (S55) in vector form:

$$|\psi_1\rangle = \frac{1}{2\sqrt{2}}(1 - i, 1 + i, 1 + 1, 1 - 1)^\top, \quad (\text{S56})$$

$$|\psi_2\rangle = \frac{1}{2\sqrt{2}}(1 - i, -1 + i, -1 + i, -1 - i)^\top. \quad (\text{S57})$$

Furthermore, we introduce two additional states

$$|\psi_3\rangle = \frac{1}{2\sqrt{2}}(-1 + i, -1 - i, 1 + i, 1 - i)^\top, \quad (\text{S58})$$

$$|\psi_4\rangle = \frac{1}{2\sqrt{2}}(1 + i, 1 - i, -1 + i, -1 - i)^\top. \quad (\text{S59})$$

The states $|\psi_j\rangle$ ($j = 1, \dots, 4$) specify the full basis for the two-qubit state in $\mathcal{H}_P \otimes \mathcal{H}_\Pi$, where \mathcal{H}_P (\mathcal{H}_Π) denote the path (polarization) Hilbert space.

2. Bell state projection scheme

We can now define the transformation corresponding to the scheme shown in Fig. S1(b):

| \mathcal{O} | S_{RR} | S_{LL} | S_{RL} | S_{LR} |
|---|---|--|---|---|
| $\sigma_x^{\mathcal{P}} \sigma_x^{\Pi}$ | $\frac{1}{\sqrt{2}} \mathbb{I}^{\Pi}$ | $\frac{1}{\sqrt{2}} \sigma_x^{\Pi}$ | $-\frac{i}{\sqrt{2}} \sigma_x^{\Pi}$ | $\frac{1}{\sqrt{2}} \mathbb{I}^{\Pi}$ |
| $\sigma_y^{\mathcal{P}} \sigma_z^{\Pi}$ | $\frac{1}{\sqrt{2}} \sigma_x^{\Pi}$ | $\frac{1+i}{2\sqrt{2}} (\sigma_x^{\Pi} + \sigma_y^{\Pi})$ | $-\frac{1}{\sqrt{2}} \sigma_y^{\Pi}$ | $\frac{1+i}{2\sqrt{2}} (\sigma_x^{\Pi} - \sigma_y^{\Pi})$ |
| $\sigma_z^{\mathcal{P}} \sigma_y^{\Pi}$ | $\frac{1}{2\sqrt{2}} (-i\mathbb{I}^{\Pi} + \sigma_x^{\Pi} - i\sigma_y^{\Pi} + i\sigma_z^{\Pi})$ | $\frac{1}{2\sqrt{2}} (\mathbb{I}^{\Pi} - i\sigma_x^{\Pi} + \sigma_y^{\Pi} + \sigma_z^{\Pi})$ | $\frac{1}{2\sqrt{2}} (-\mathbb{I}^{\Pi} - i\sigma_x^{\Pi} + \sigma_y^{\Pi} - \sigma_z^{\Pi})$ | $\frac{1}{2\sqrt{2}} (-i\mathbb{I}^{\Pi} - \sigma_x^{\Pi} + i\sigma_y^{\Pi} + i\sigma_z^{\Pi})$ |

Table III. Components of the unitary 2-qubit gate defined in Eq. (S41) which maps the four eigenstates of the 2-qubit observable \mathcal{O} to the four output ports D_1, \dots, D_4 in Fig. S1(d).

| \mathcal{O} | V_1 | α | β | γ | δ | V_L | α | β | γ | δ | V_R | α | β | γ | δ | V_2 | α | β | γ | δ |
|---|--------------------|------------------|-------------------|------------------|------------------|--|------------------|------------------|-----------------|-------------------|--|------------------|------------------|-----------------|------------------|---|------------------|-----------------|------------------|------------------|
| $\sigma_x^{\mathcal{P}} \sigma_x^{\Pi}$ | σ_x^{Π} | 0 | $\frac{\pi}{4}$ | 0 | $\frac{\pi}{2}$ | $e^{i\frac{\pi}{4}} \sigma_x^{\Pi}$ | 0 | $\frac{\pi}{4}$ | 0 | $\frac{3\pi}{4}$ | $e^{-i\frac{\pi}{4}} \sigma_x^{\Pi}$ | 0 | $\frac{\pi}{4}$ | 0 | $\frac{\pi}{4}$ | \mathbb{I}^{Π} | 0 | 0 | 0 | π |
| $\sigma_y^{\mathcal{P}} \sigma_z^{\Pi}$ | $-i\sigma_z^{\Pi}$ | 0 | 0 | $\frac{\pi}{2}$ | 0 | $\frac{i}{\sqrt{2}} (\sigma_x^{\Pi} + \sigma_y^{\Pi})$ | $-\frac{\pi}{4}$ | $\frac{3\pi}{8}$ | $\frac{\pi}{4}$ | $-\pi$ | $\frac{1}{\sqrt{2}} (\sigma_x^{\Pi} + \sigma_y^{\Pi})$ | $-\frac{\pi}{4}$ | $-\frac{\pi}{8}$ | $\frac{\pi}{4}$ | $-\frac{\pi}{2}$ | $\frac{1-i}{2} \mathbb{I}^{\Pi} - \frac{1+i}{2} \sigma_z^{\Pi}$ | $-\frac{\pi}{4}$ | $\frac{\pi}{8}$ | $-\frac{\pi}{4}$ | $-\frac{\pi}{4}$ |
| $\sigma_z^{\mathcal{P}} \sigma_y^{\Pi}$ | $\tilde{\sigma}_1$ | $-\frac{\pi}{4}$ | $-\frac{7\pi}{8}$ | $-\frac{\pi}{2}$ | $\frac{7\pi}{4}$ | $\tilde{\sigma}_L$ | $-\frac{\pi}{4}$ | $-\frac{\pi}{4}$ | π | $-\frac{3\pi}{4}$ | $\tilde{\sigma}_R$ | $-\frac{\pi}{4}$ | $-\frac{\pi}{4}$ | $\frac{\pi}{2}$ | $\frac{3\pi}{4}$ | $\frac{1+i}{2} (\sigma_x^{\Pi} - \sigma_y^{\Pi})$ | $-\frac{\pi}{4}$ | $\frac{\pi}{8}$ | $\frac{\pi}{4}$ | $\frac{3\pi}{4}$ |

Table IV. Configuration of the angles of the HWP, QWPs, and phase shifter to measure the entanglement witnesses defined in Eqs. (S65) and (S66). For the longer expressions we have introduced the notation $\tilde{\sigma}_1 = \frac{1-i}{2} \mathbb{I}^{\Pi} + \frac{1+i}{2} \sigma_y^{\Pi}$, $\tilde{\sigma}_L = \frac{1+i}{2\sqrt{2}} \mathbb{I}^{\Pi} + \frac{1-i}{2\sqrt{2}} (\sigma_x^{\Pi} + \sigma_y^{\Pi} + \sigma_z^{\Pi})$, and $\tilde{\sigma}_R = \frac{1-i}{2\sqrt{2}} \mathbb{I}^{\Pi} + \frac{1+i}{2\sqrt{2}} (-\sigma_x^{\Pi} + \sigma_y^{\Pi} + \sigma_z^{\Pi})$.

$$\mathcal{U}_{\mathcal{B}} = U_{\text{PBS}} \begin{bmatrix} U_{\text{QWP}}(\pi/4) & 0 \\ 0 & U_{\text{QWP}}(\pi/4) \end{bmatrix} \quad (\text{S60})$$

where U_{PBS} and $U_{\text{QWP}}(\pi/4)$ are defined in Eqs. (S10) and (S28), respectively. We find

$$U_{\mathcal{B}}|\psi_1\rangle = \frac{e^{-i\frac{\pi}{4}}}{\sqrt{2}} (1, 1, 0, 0)^{\top}, \quad (\text{S61})$$

$$U_{\mathcal{B}}|\psi_2\rangle = -\frac{e^{-i\frac{\pi}{4}}}{\sqrt{2}} (0, 0, 1, 1)^{\top}, \quad (\text{S62})$$

$$U_{\mathcal{B}}|\psi_3\rangle = -\frac{e^{-i\frac{\pi}{4}}}{\sqrt{2}} (1, -1, 0, 0)^{\top}, \quad (\text{S63})$$

$$U_{\mathcal{B}}|\psi_4\rangle = -\frac{e^{-i\frac{\pi}{4}}}{\sqrt{2}} (0, 0, 1, -1)^{\top}, \quad (\text{S64})$$

where the global phase factors are not important here. The detector B_j ($j = 1, \dots, 4$) in Fig. S1(b) will thus give a maximum signal when we are in the Bell state $|\psi_j\rangle$ ($j = 1, \dots, 4$), while the other three detectors will show a null signal. In our specific experimental configuration we see that the detectors B_1 and B_2 can thus identify the two Bell states $|\psi_1\rangle$ and $|\psi_2\rangle$, respectively, as shown in Fig. S1(c).

3. Construction of optimal entanglement witness

Fidelity-based entanglement witnesses such as those constructed in Sec. D can thus be constructed,

$$\mathcal{W}_1 = \frac{1}{4} [I - \sigma_x^{\mathcal{P}} \sigma_x^{\Pi} - \sigma_y^{\mathcal{P}} \sigma_z^{\Pi} - \sigma_z^{\mathcal{P}} \sigma_y^{\Pi}], \quad (\text{S65})$$

$$\mathcal{W}_2 = \frac{1}{4} [I - \sigma_x^{\mathcal{P}} \sigma_x^{\Pi} + \sigma_y^{\mathcal{P}} \sigma_z^{\Pi} + \sigma_z^{\mathcal{P}} \sigma_y^{\Pi}], \quad (\text{S66})$$

for $|\psi_1\rangle, |\psi_2\rangle$, respectively. These observables successfully detect entanglement in a white-noise affected state provided the probability of preparing the desired states satisfies $p > 1/3$.

4. Measuring entanglement witnesses using the universal unitary gate

To implement the entanglement witnesses in Eqs. (S65) and (S66) we employ the universal unitary gate for single-photon two-qubit states [48] shown in Fig. S1(d). The configuration of the universal unitary gate is detailed in Tables III and IV.

G. Robustness estimates

We quantify the effect of imperfections and losses on the possibility of witnessing entanglement. We will first focus on the double-loop scheme presented in Fig. 1, where the optimal entanglement witnesses are defined in Eqs. (S36) and (S37). To estimate the robustness of the double-loop scheme with respect to the main experimental parameters we introduce the test vector

$$|\tilde{\psi}\rangle = \frac{1}{2} \left(e^{-\frac{iL_a n_1 \omega}{c} - \frac{iL_a r_a \Omega \omega}{c^2}}, e^{\frac{iL_a r_a \Omega \omega}{c^2} - \frac{iL_a n_2 \omega}{c}}, e^{-\frac{iL_b n_1 \omega}{c} - \frac{iL_b r_b \Omega \omega}{c^2}}, e^{\frac{iL_b r_b \Omega \omega}{c^2} - \frac{iL_b n_2 \omega}{c}} \right)^{\top}, \quad (\text{S67})$$

for evaluating the expectation value of $\langle \tilde{\psi} | \mathcal{W}_1 | \tilde{\psi} \rangle$ and $\langle \tilde{\psi} | \mathcal{W}_2 | \tilde{\psi} \rangle$. The state $|\tilde{\psi}\rangle$ takes into account possible variations from the ideal experimental parameters: L_a (L_b) denote the total length of the small (big) loops of radius r_a (r_b), and n_1 (n_2) denote the refractive index for the slow (fast) axis. We set the unperturbed parameters to the following values: radius $r_b = 0.5$ m, winding number

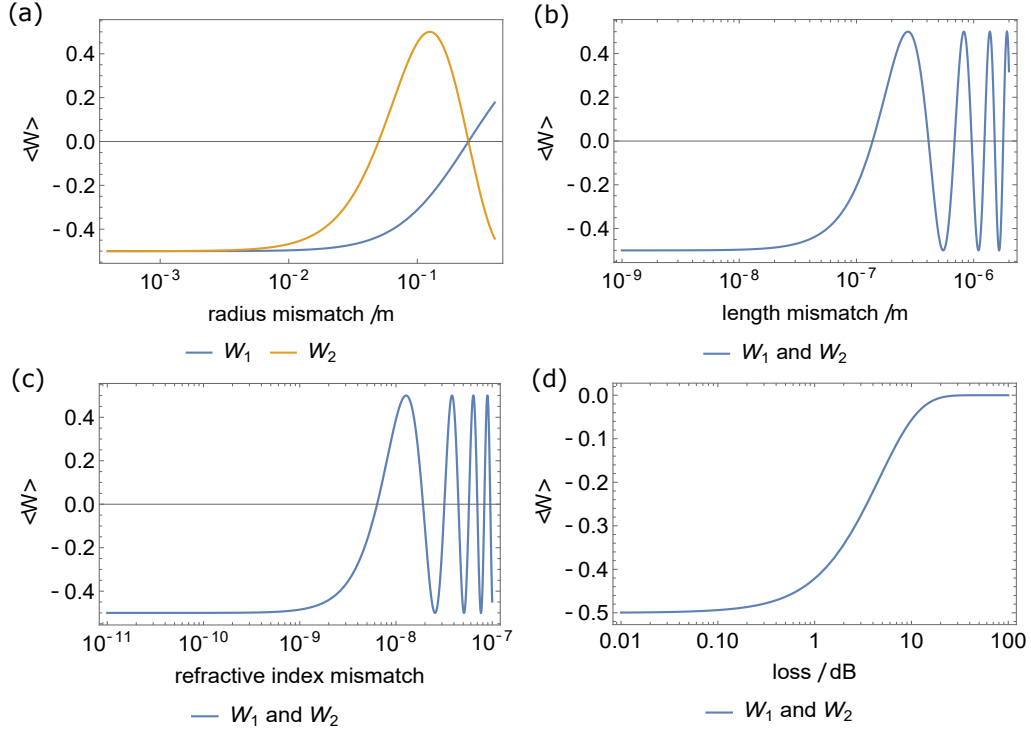


Figure S2. Variation of the expectation values of the entanglement witnesses $\langle W_1 \rangle$ and $\langle W_2 \rangle$ due to imperfections and losses for the double-loop scheme. For the single-loop scheme we find similar estimates for (c), (d), while (a), (b) become redundant. The unperturbed parameters are: big radius $r_b = 0.5\text{m}$, small radius $r_a = r_b/2$, winding number for big (small) loop $N_b = 10$ ($N_a = 20$) corresponding to the length of the individual loops of about $\sim 31.5\text{m}$, refractive index $n = 1.456$, and photon wavelength $\lambda = 800\text{nm}$. (a) Tolerance on the radius (δr) with perfect length matching. We consider variations of the radius $r_b + \delta r$, but we obtain similar tolerances for the variation of the radius r_a . (b) Length mismatch between the two fiber loops ($\delta L = L_b - L_a$). (c) Mismatch of the refractive index for the two polarization ($\delta n = n_2 - n_1$). (d) Losses in the four fiber paths. Comparable experimental tolerances have been recently achieved in [16]. Given an initial non-zero mismatch in the refractive index (a), the radius (b), and the path length (d) one would not require recalibration, but can still perform the experiment as discussed in the main text. This would in general result in the shifted origin of Figs. 1(c) and 1(e), as the effect of entanglement generation would still exhibit the same periodicity $4\Omega_{\text{Bell}}$ (see Eqs. (10) and (11)).

$N_b = 10$ corresponding to the length of the individual loops of about ~ 31.5 m, refractive index $n = 1.456$, and photon wavelength $\lambda = 800$ nm. We show how $\langle \tilde{\psi} | \mathcal{W}_1 | \tilde{\psi} \rangle$ and $\langle \tilde{\psi} | \mathcal{W}_2 | \tilde{\psi} \rangle$ depend on imperfections in Fig. S2 (a), (b), and (c).

We now quantify the effect of losses on the optimal entanglement witness \mathcal{W}_1 but an analogous analysis can be performed also for \mathcal{W}_2 . We set the frequency to the optimal value $\Omega = \Omega_{\text{Bell}}$ such that the test vector in Eq. (S67) reduces to

$$|\tilde{\psi}\rangle = \frac{1}{2}(-i, i, -1, -1)^\top. \quad (\text{S68})$$

We suppose the loss can occur in any of the four paths with probability p . For example, a single channel loss in the path a and polarization H would produce the state

$$|\tilde{\psi}_{aH}\rangle = \frac{1}{\sqrt{3}}(0, i, -1, -1)^\top. \quad (\text{S69})$$

with similar definitions for the other three channels aV , bH , bV . The loss in two channels (aH , bH) would occur with probability p^2 , resulting in the state

$$|\tilde{\psi}_{aH,aV}\rangle = \frac{1}{\sqrt{2}}(0, 0, -1, -1)^\top, \quad (\text{S70})$$

with analogous definitions for the channels (aH , bH), (aH , bV), (aV , bH), (aV , bV), (bH , bV). Finally, the three channel loss (aH , aV , bH) would occur with probability p^3 , with the associated state given by:

$$|\tilde{\psi}_{aH,aV,bH}\rangle = (0, 0, 0, -1)^\top, \quad (\text{S71})$$

with again similar definitions for the other cases (aH , aV , bV), (aH , bH , bV), (aV , bH , bV). To compute the expectation value of the entanglement witness we need to average over the four types of states defined in Eqs. (S68)-(S71); no loss with probability $1 - (4p + 6p^2 + 4p^3)/14$, single channel loss with probability $p/14$ (4 different states), two channel loss with probability $p^2/14$ (6

different states), and three channel loss with probability $p^3/14$ (4 different states). In other words, we construct the density matrix:

$$\begin{aligned} \rho = & \left(1 - \frac{4p + 6p^2 + 4p^3}{14}\right) |\tilde{\psi}\rangle\langle\tilde{\psi}| + \frac{p}{14} \sum_j |\tilde{\psi}_j\rangle\langle\tilde{\psi}_j| \\ & + \frac{p^2}{14} \sum_{j,l} |\tilde{\psi}_{jl}\rangle\langle\tilde{\psi}_{jl}| + \frac{p^3}{14} \sum_j |\tilde{\psi}_{jlm}\rangle\langle\tilde{\psi}_{jlm}| \quad (\text{S72}) \end{aligned}$$

where j, l, m denote a loss channel aH, aV, bH, bV . We show how the value of $\langle\mathcal{W}_j\rangle = \text{tr}[\rho\mathcal{W}_j]$ ($j = 1, 2$) is attenuated in Fig. 1(d).

An similar analysis of imperfections and losses, discussed above for the double-loop scheme, can be also applied to the single-loop scheme shown in Fig. S1.

We consider the constructed entanglement witnesses in Eqs. (S65) and (S66) and introduce the test vector

$$|\tilde{\psi}\rangle = \frac{1}{2} \left(e^{-\frac{iLr\omega\Omega}{c^2} - \frac{iLn_1\omega}{c}}, e^{\frac{iLr\omega\Omega}{c^2} - \frac{iLn_2\omega}{c}} \right. \\ \left. e^{\frac{iLr\omega\Omega}{c^2} - \frac{iLn_1\omega}{c}}, e^{-\frac{iLr\omega\Omega}{c^2} - \frac{iLn_2\omega}{c}} \right)^\top, \quad (\text{S73})$$

which is used for evaluating the expectation values, $\langle\tilde{\psi}|\mathcal{W}_1|\tilde{\psi}\rangle$ and $\langle\tilde{\psi}|\mathcal{W}_2|\tilde{\psi}\rangle$. We find that the tolerance on the mismatch of the refractive index for the two polarizations ($\delta n = n_2 - n_1$) is comparable to the computed for the double loop scheme in Fig. S2(c), and a similar attenuation of the entanglement witness with losses to the one shown Fig. S2(d). On the other hand, the single-loop scheme is no longer susceptible to radius and length mismatch, as the scheme relies on a single fiber loop, and hence Fig. S2(a) and Fig. S2(b) become redundant.